

Experimental and Theoretical Analysis of Drag Forces in Micromechanical-Beam Arrays

Ashok Akarapu,^{1,†} Rohit Prakash Nighot,^{1,†} Lalsingh Devsoth,¹ Mukul Yadav,¹ Prem Pal,² and Ashok Kumar Pandey^{1,*}

¹*Department of Mechanical and Aerospace Engineering, Indian Institute of Technology Hyderabad, Kandi, Sangareddy, 502285 TS, India*

²*Department of Physics, Indian Institute of Technology Hyderabad, Kandi, Sangareddy, 502285 TS, India*

 (Received 18 February 2019; revised manuscript received 14 July 2019; accepted 14 February 2020; published 2 March 2020)

Computation of drag force due to oscillation of a beam or any other solid structure near or away from the fixed surface is very important in controlling the performance of most microelectromechanical and nanoelectromechanical systems. Although there exist many formulations for drag-force computations near and away from the fixed bottom surface, they are limited to a single element. In this paper, we present a systematic formulation for arriving at a modified formula for drag force based on experimental and numerical simulations that can be used in computing forces in an array of microelectromechanical and nanoelectromechanical system beams. To develop the model, we first obtain an approximate analytical model for uniform as well as nonuniform motion of a cantilever beam. After validating the numerical model with experimental and analytical results for a single beam, we modify the formula to consider different boundary effects and then apply it to compute drag forces in an array of beams. Finally, we also modify the formulas to include the nearby wall effect. The formula developed works excellently when the interbeam gaps are small. However, the percentage error increases with interbeam gap and is found to be between 5% and 14%.

DOI: [10.1103/PhysRevApplied.13.034003](https://doi.org/10.1103/PhysRevApplied.13.034003)

I. INTRODUCTION

With the growing need for realizing high-bandwidth devices for imaging and characterization [1,2], the focus has shifted toward utilizing microelectromechanical system (MEMS) and nanoelectromechanical system (NEMS) arrays [3,4]. Recently, researchers have been exploring an array of microcantilevers of different materials to improve the performance of MEMS-based sensors and actuators. Walters *et al.* [5] have investigated an array of silicon nitride cantilevers having different lengths ranging from 23 to 203 μm for application in atomic force microscopy (AFM). Schneider *et al.* [6] demonstrated parallel imaging of large sample areas using arrays of polymer SU-8 microcantilevers. They have investigated cantilevers with different SU-8 thicknesses. Using an array of five AFM microcantilevers, Somnath *et al.* [7] demonstrated parallel topographic imaging and nanolithography. In another study, to improve the size of measurement area and scan speed, Seong *et al.* [8] proposed an array of 30 microcantilevers in order to acquire an image of size $0.510 \times 0.425 \text{ mm}^2$, which is much larger than a conventional AFM

image. Further, Maris *et al.* [9] presented a new design consisting of arrays of piezoresistive cantilevers for large-area imaging in air as well as liquid. Although there are many studies utilizing arrays of cantilevers, the various coupling effects have been ignored. Most coupled field analyses in microelectromechanical cantilever beam arrays are limited to structural and electrical coupling effects in frequency tuning. In this paper, we develop a model to compute drag forces that can be used to study fluid-structure interaction in microcantilever beams arrays and can be further utilized in improving the performance of many devices such as the scanning characteristics of AFM cantilevers in biological applications, the frequency bandwidth of energy harvesters, the switching characteristics of array-based MEMS devices, etc.

Microcantilever structures operating in ambient conditions are mostly damped due to fluid-based damping mechanisms such as squeeze-film damping and drag forces [10]. While the squeeze-film damping dominates when the vibrating structure is very close to a fixed wall, the damping due to drag forces is common when the vibrating structures are away from the fixed surfaces. As the drag force has been historically significant in understanding various fluid-structure interaction phenomena, we perform numerical and analytical analyses of drag forces in single

*ashok@iith.ac.in

†These authors contributed equally.

as well as arrays of MEMS structures with or without nearby wall. A few decades ago, Landau and Lifshitz [11] presented a theoretical analysis of the drag on a vibrating sphere under the assumption of low Reynolds number. Ikehala *et al.* [12] studied the influence of size and mode effect on the drag forces. They found that the quality factors based on drag forces are a strong function of length, width, and mode shapes. Verbridge *et al.* [13] measured the quality factor by varying the gap as well as width of the beam. They found that the quality factor first increases with an increase in beam width and then starts decreasing. Recently, Vishwakarma *et al.* [14] quantified the interplay of damping due to drag force and squeeze film as the beam width increases. They found that the drag force dominates the squeeze film when the width is very small, and the squeeze film takes over for larger widths. Newell [15] presented a frequency-independent approximate expression for the quality factor based on the drag forces in a rectangular beam. Bullard *et al.* [16] obtained the drag-force formula based on similarity laws. Sader [17] presented a detailed theoretical analysis of a vibrating cantilever beam immersed in a fluid. He expressed the fluid forces in terms of a complex hydrodynamic function to quantify the drag forces and mass loading effect. Maali *et al.* [18] systematically computed the values of constants associated with the hydrodynamic function used in the drag force by curve-fitting the numerical results for a beam with rectangular cross section. Xia and Li [19] compared the computed and measured values of drag forces on a beam by converting it into a dish-string model. They studied the influence of flexural as well as torsional mode on drag forces. Zhang and Turner [20] developed a theoretical model of drag force and added mass effect based on the theory presented by Landau and Lifshitz [11]. After finding an expression for the forces, they validated the theoretical model with experimental results. Subsequently, they developed a numerical model to find the drag forces due to the vibration of beams with different cross-section shape such as rectangular, elliptical and circular. They found that the difference in damping coefficients due to change in cross section is less than 5% [21]. Moreover, they mentioned that the effect of beam width on its thickness ratio on damping becomes invariable if its ratio is more than 5. However, all the above approaches are used to find drag forces in a single beam of different shapes and sizes. To obtain the drag force in a multibeam array, Basak and Raman [22] solved the unsteady Stokes equation using a boundary integral technique to obtain the numerical simulation. They described the influence of the hydrodynamic coupling on damping and added mass effects as a function of frequency, gap, and relative phase and amplitude of two nearby beams [22]. Although the model is very important in finding drag forces in an array of beams, it is not very straightforward to apply. Hence, we focus on developing a simple empirical model based on experimental and numerical simulation

that can be used to compute drag forces in an array of multibeam with or without lower wall.

In this paper, we first fabricate a single cantilever beam and arrays of two and three beams using a wet-etching process [23]. We measure frequencies and quality factor of beams using a Polytec laser vibrometer in ambient and vacuum. Then, using the drag-force model for uniform motion of a rigid cylinder developed by Zhang and Turner [20], we first develop an analytical model for computing drag forces in a cantilever beam with approximate mode shape. We compare the results with experimental and numerical models. On validating the numerical models with analytical results in a beam executing rigid motion as well as flexural motion, respectively, we modify the formula based on numerical simulation so as to compute forces in the beam array system. We also show the influence of the nearby wall on the drag force due to oscillatory motion of the beam.

II. EXPERIMENTAL RESULTS AND ANALYSIS

In the present work, single beams and arrays (double and triple) of silicon dioxide (SiO_2) micromechanical beams were fabricated to validate numerical and analytical results relating to quality factor, Q . The micromechanical beams were fabricated using wet bulk micromachining in 25-wt% tetramethylammonium hydroxide at 75°C . The step-by-step fabrication process is explained in our previous work [23]. The length, width, and thickness of the micromechanical beams are 200, 40, and $0.965\ \mu\text{m}$, respectively. Each beam is separated by $60\ \mu\text{m}$ from the bottom. Furthermore, the side gap (distance from beam to side) is varied in order to investigate the influence of side gap and inter-beam gaps on damping characteristics of micromechanical beams. A laser scanning vibrometer (Polytec OFV-5000) whose experimental setup is explained elsewhere [23] was utilized to investigate the resonance frequency of cantilever beams. In one set of beams the gaps from beam to all sides (s_1 and s_2) are fixed equal, whereas in another set the gaps from beam to two sides (s_2) are fixed as equal and the gap from beam to the third free side (s_1) is fixed at $80\ \mu\text{m}$. For instance, Figs. 1(a)–1(c) illustrate the optical micrographs and frequency response corresponding to the first transverse mode of single, double, and triple SiO_2 micromechanical cantilever beams of equal side gap on two sides ($s_2 = 24\ \mu\text{m}$) and gap (s_1) $80\ \mu\text{m}$ on the third side. The resonance frequency is found to be about 21.2 kHz. Additionally, the spectra of a single point on the free ends of beam 1 and beam 2 in a two-beam array under ambient conditions are shown in Fig. 2(c). It is noted that both look nearly identical but there is a small difference in their amplitudes. Therefore, the average frequency spectrum of all the points on both beams will be dominated by beam 1 that looks similar to its response as shown in Fig. 2(d). Similarly, individual frequency spectra of a

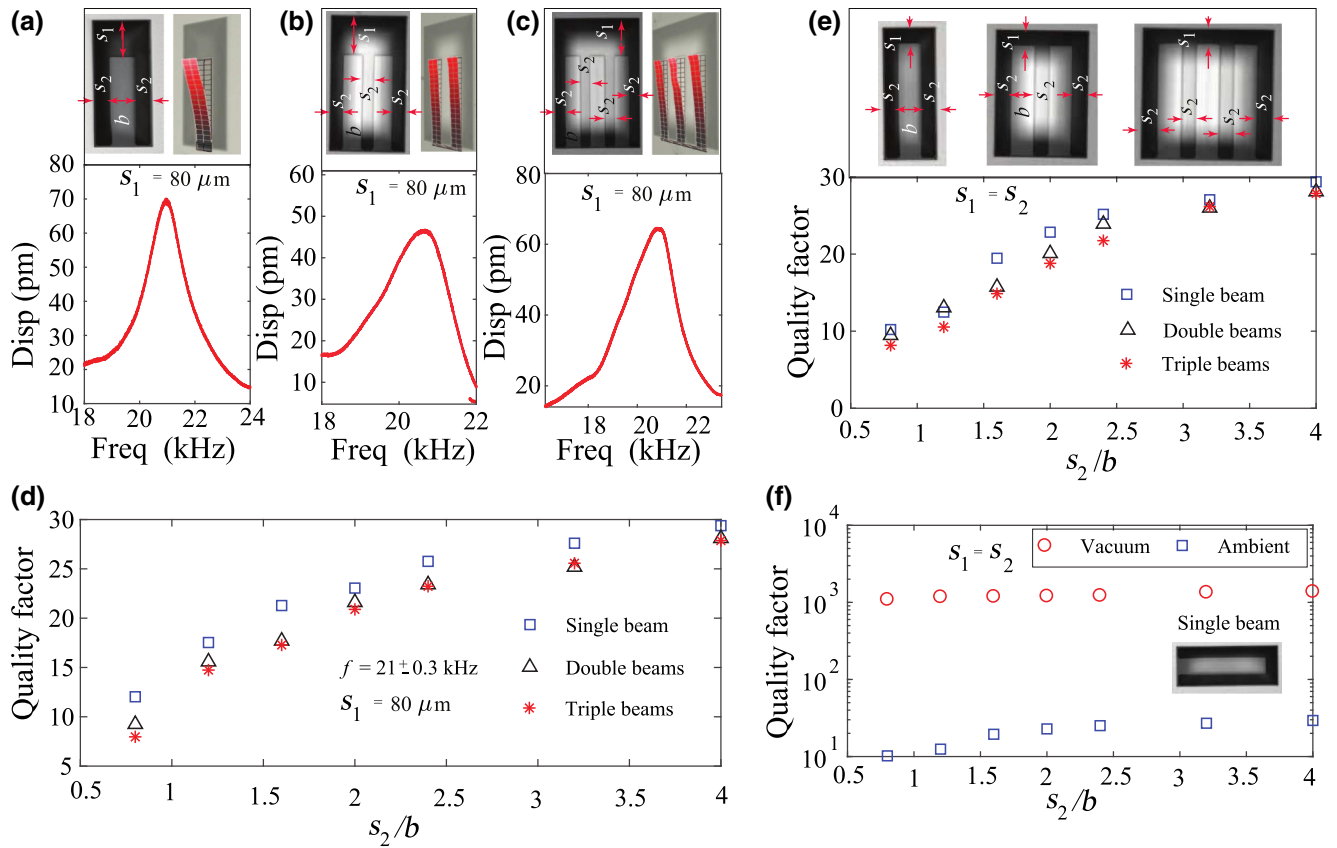


FIG. 1. Images and averaged frequencies of (a) single cantilever beam, (b) two-beam array, and (c) three-beam array with two equal side boundaries of gap s_2 and different third side boundary s_1 . Variation of quality factors of all the three types of beam for beams with (d) unequal side boundaries and (e) equal side boundaries. (f) Variation of quality factor of single beam with equal side boundaries under ambient and vacuum conditions.

single point at the free end of beams 1, 2, and 3 of a three-beam array are slightly different in terms of peak frequencies as well as amplitudes, as shown in Fig. 2(g). It is also observed that the spectra of beam 1 and beam 3 show some coupling effect due to the large vibrational amplitude of beam 2. Therefore, the average frequency spectrum of all the points of three-beam arrays is mainly dominated by beams 2 and 1 as shown in Fig. 2(h). However, the spectra of coupled beams under vacuum conditions show that two modes (in-phase and out-of-phase modes) of two coupled beams are found to be separated by around 0.2 kHz as shown in Figs. 2(a) and 2(b). Such differences disappear under ambient conditions and give coupled responses. As we increase the number of beams to three in a three-beam array, the frequency band over the three modes of the three-beam array spreads over 0.4 kHz under vacuum conditions as shown in Figs. 2(e) and 2(f). However, these modes disappear under ambient condition and give a single transverse coupled response.

Based on the above analysis, we find that the fluid coupling in single beams as well as multibeam arrays influences frequencies as well as fluid damping. While

the frequency reduces due to the added mass effect of fluid-structure coupling and interactions, it increases the damping in single beams as well as beam arrays as the surrounding conditions vary from vacuum to ambient. However, it is found that the reduction in frequency is negligible in the present case. Therefore, the focus here is on computing damping in single beams as well as multibeam arrays. It is also important to note that although the frequency response curves of individual beams in two- and three-beam arrays are close to each other under ambient conditions, they appear to be uncoupled and sufficiently separated from each other under vacuum conditions. The separate frequencies of individual beams under vacuum conditions are due to structural coupling due to overhanging effects near the support of two- and three-beam arrays.

To describe this structural and damping coupling in multibeam arrays, we consider a two-beam array having similar beams with effective masses m_1 and m_2 , effective stiffnesses k_1 and k_2 , and effective damping coefficients b_1 and b_2 that are coupled through coupled stiffness k_c and coupled damping coefficient b_c . The equation of

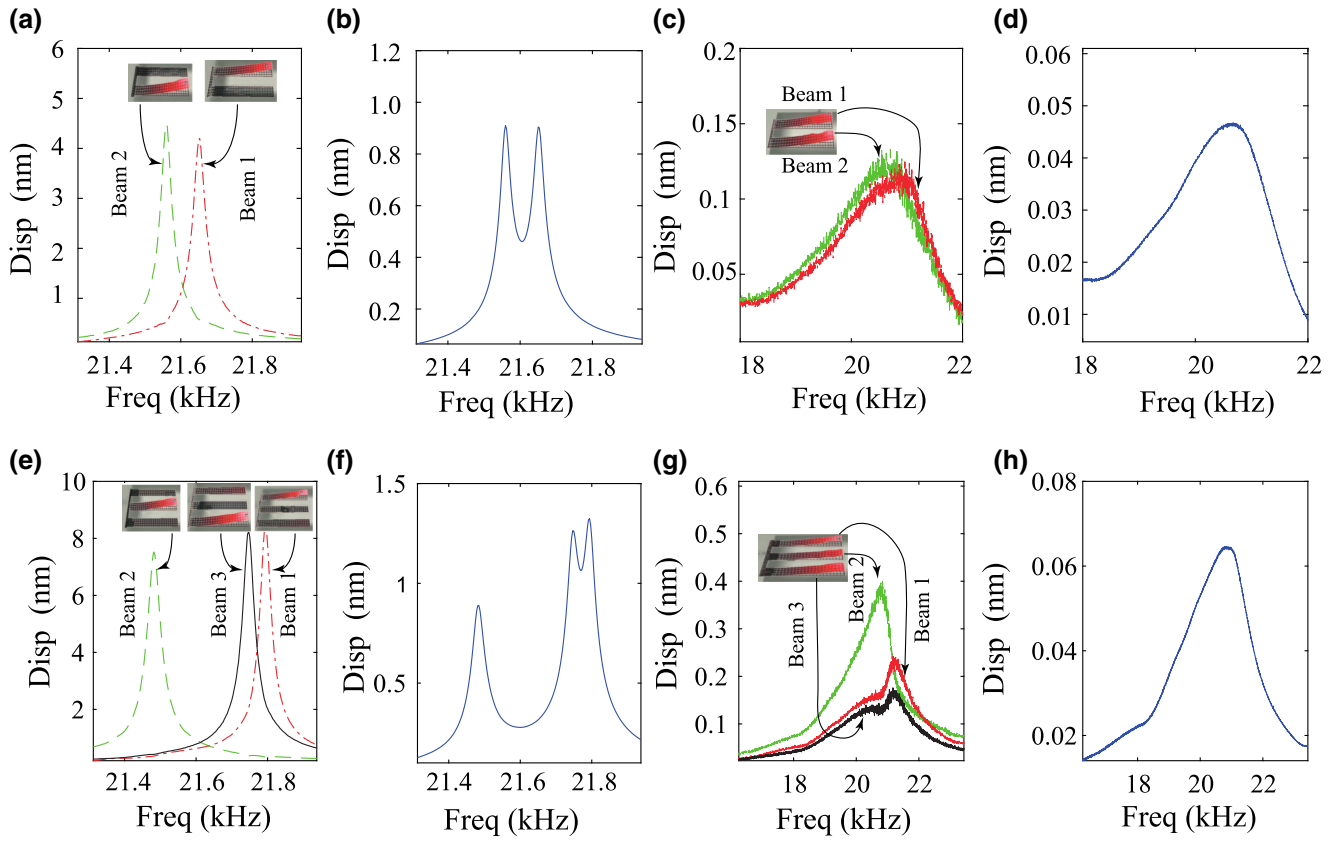


FIG. 2. (a) Frequency response of individual beams of two-beam array in a vacuum. (b) Averaged frequency response of two-beam array under vacuum. (c) Frequency response of individual beams of two-beam array under ambient conditions. (d) Averaged frequency response of two-beam array under ambient conditions. (e) Frequency response of individual beams of three-beam array under vacuum. (f) Averaged frequency response of three-beam array under vacuum. (g) Frequency response of individual beams of three-beam array under ambient conditions. (h) Averaged frequency response of three-beam array under ambient conditions.

motion of two beams under free vibration and considering the Kelvin-Voigt viscoelastic model [24] can be written as

$$\begin{aligned} \ddot{q}_1(t) + \frac{b_1}{m_1} \dot{q}_1 + \frac{k_1}{m_1} q_1 + \frac{k_c}{m_1} (q_1 - q_2) + \frac{b_c}{m_1} (\dot{q}_1 - \dot{q}_2) &= 0, \\ \ddot{q}_2(t) + \frac{b_2}{m_2} \dot{q}_2 + \frac{k_2}{m_2} q_2 + \frac{k_c}{m_2} (q_2 - q_1) + \frac{b_c}{m_2} (\dot{q}_2 - \dot{q}_1) &= 0. \end{aligned} \quad (1)$$

To find the influence of coupling on frequencies, let us use free and undamped vibration of beams, but for the time being retaining coupled damping b_c . For simplicity and due to symmetric conditions of similar beams under bending, we can assume $m_1 = m_2 = m$ and $k_1 = k_2 = k$, $\omega_{12}^2 = \omega_{21}^2 = k_c/m$, and rewrite the above equation as

$$\begin{aligned} \ddot{q}_1(t) + \frac{k}{m} q_1 + \frac{k_c}{m} (q_1 - q_2) + \frac{b_c}{m} (\dot{q}_1 - \dot{q}_2) &= 0, \\ \ddot{q}_2(t) + \frac{k}{m} q_2 + \frac{k_c}{m} (q_2 - q_1) + \frac{b_c}{m} (\dot{q}_2 - \dot{q}_1) &= 0. \end{aligned} \quad (2)$$

Assuming the solutions $q_1 = q_{10} \exp(-i\omega t)$, $q_2 = q_{20} \exp(-i\omega t)$ and substituting into the above equations, we get

$$\begin{aligned} \left(\frac{k}{m} + \frac{k_c}{m} - i \frac{b_c}{m} \omega - \omega^2 \right) q_{10} + \left(-\frac{k_c}{m} + i \frac{b_c}{m} \omega \right) q_{20} &= 0, \\ \left(-\frac{k_c}{m} + i \frac{b_c}{m} \omega \right) q_{10} + \left(\frac{k}{m} + \frac{k_c}{m} - i \frac{b_c}{m} \omega - \omega^2 \right) q_{20} &= 0. \end{aligned} \quad (3)$$

For a nonzero solution of $\{q_{10}, q_{20}\}^T$, the determinant of the coefficient matrix of the above equations is taken as zero. Subsequently, we get frequencies

$$\omega_1^2 = \frac{k}{m}, \quad \omega_2^2 = \frac{k}{m} + 2 \frac{k_c}{m} - 2i \frac{b_c}{m}. \quad (4)$$

Thus, it is shown that due to coupled damping coefficients, one of the frequencies becomes a complex number. The difference in the frequency is found to be due to coupled stiffness k_c and coupled damping coefficients b_c . The coupled effect of damping on two resonators with viscoelastic

assumption is also discussed by Gattulli *et al.* [24] and that with inelastic assumption is discussed by Dolfo and Vigué [25]. The effects of coupled stiffness on beam arrays without damping effect have also been discussed extensively by many researchers [23,26,27].

Under vacuum conditions, fluid coupling between the beams can be negligible, as can be observed in Figs. 2(a) and 2(b) in which the frequency responses of individual beams are clearly found to be unaffected by the response of the other beam; thus we can take $b_c = 0$. Consequently, we find two frequencies corresponding to two different modes ϕ_1 and ϕ_2 in terms of coupled stiffness k_c [23]:

$$\omega_1 = \sqrt{\frac{k}{m}}, \quad \omega_2 = \sqrt{\frac{k + 2k_c}{m}}. \quad (5)$$

However, based on the experimental results for the two-beam array under vacuum conditions, for $m = \frac{33}{140}m_{\text{tot}} = 4.03 \times 10^{-12}$ kg, we find $k = 7.3 \times 10^{-2}$ N/m and $k_c = 3.2 \times 10^{-4}$ N/m. Similarly, for the three-beam array [23], using $\omega_1 = \sqrt{k/m}$, $\omega_2 = \sqrt{(k + k_c)/m}$, and $\omega_3 = \sqrt{(k + 3k_c)/m}$, we obtain $k = 7.3 \times 10^{-2}$ N/m and $k_c = 7.1 \times 10^{-4}$ N/m. A relatively small value of k_c is found due to very small structural coupling between the beams due to overhang induced due to underthings. Consequently, these frequencies are very close to each other. Since the frequency response curves of two beam arrays in a vacuum is found to be uncoupled, the quality factor can be found from the half-width method and the damping ratio corresponding to each beam with corresponding frequency ω_r can be found from $Q_r = 1/2\xi_r$, where r represents the r th beam as described below.

Now, for the modal vector $u_r = \{\phi_1, \phi_2, \dots\}^T$ corresponding to the above frequencies ω_r , Eqs. (2) with external excitation force $Q = Q_0 \exp(i\Omega t)$ with excitation frequency Ω are transformed into a modal dynamic equation using modal vector $u_r = \{\phi_1, \phi_2, \dots\}^T$ by assuming $q(t) = \sum_r \eta_r(t)u_r$ and using orthogonal properties of modal vectors [28,29]:

$$\ddot{\eta}_r + 2\xi_r\omega_r\dot{\eta}_r + \omega_r^2\eta_r = N_r = u_r^T Q_0 \exp(i\Omega t), \quad (6)$$

where r is the number of first transverse modes corresponding to different beams. For example, for a two-beam array, $r = 1, 2$, and for a three-beam array, $r = 1, 2, 3$. The corresponding frequency response can be written as $G_r(i\Omega) = |G_r(i\Omega)|e^{-i\theta_r}$, where the magnitude of the frequency response curve and the frequency phase response can be found from [28]:

$$|G_r(i\Omega)| = \frac{1}{\sqrt{[1 - (\Omega/\omega_r)^2]^2 + (2\xi_r\Omega/\omega_r)^2}},$$

$$\theta_r = \arctan \frac{2\xi_r\Omega/\omega_r}{1 - (\Omega/\omega_r)^2}. \quad (7)$$

Finally, we get $q(t) = \sum_r \eta_r(t)u_r = \sum_r (u_r^T Q_0 / \omega_r^2) |G_r(i\Omega)| u_r e^{-i(\Omega t - \theta_r)}$. Thus, for each individual frequency response of two- or three-beam arrays under vacuum conditions, damping can be found by applying a single-degree-of-freedom model in reduced-order form of the equation. Thus, the quality factor can be found from the half-width method given by $Q_r = 2\pi(\omega_r / \Delta\omega_r) \approx 1/2\xi_r$ for each beam, where ξ_r is the damping ratio of the r th beam corresponding to frequency ω_r in an n -beam array.

Under ambient conditions, the frequency response is affected by the neighboring beams; however, the frequencies of beam arrays become nearly the same due to fluid damping. Therefore, in this paper, we focus on computing the damping due to fluid under ambient conditions in single arrays as well as beam arrays from the combined and average frequency response based on the half-width method. The frequencies of different beams are considered in the range of 21 ± 0.3 kHz. Figure 1(d) shows the variation of the Q factor of single, double and triple beams for side gaps, s_2 , of 16, 24, 32, 40, 48, 64, and 80 μm under ambient pressure and temperature conditions. Figure 1(e) illustrates the optical micrographs and quality factor corresponding to the first transverse mode of single, double, and triple SiO_2 micromechanical cantilever beams with equal side gaps on all three sides ($s_1 = s_2 = 24 \mu\text{m}$). Figure 1(f) shows the comparison of quality factors under ambient and vacuum conditions for different gaps between the beams. As the gap s_2 increases from 0.5 to 4 times the beam width, b , the quality factor under ambient conditions increases until $s_2/b = 2$ and then becomes independent of the gap. However, the quality factor under vacuum conditions (10^{-2} mbar) remains nearly independent of the gap between the beams. In the next two sections, we develop numerical and analytical models to compute quality factors versus side gaps s_2 in single beams as well as arrays of beams with constant end gap $s_1 = 80 \mu\text{m}$.

In order to perform numerical analysis, we first characterize the flow conditions in the test structure. Taking $\mu = 1.8 \times 10^{-5}$ Ns/m², $\rho_a = 1.2$ kg/m³, and the mean free path $\lambda_a = 67$ nm of air, the boundary layer thickness $\delta = \sqrt{2\mu/\rho_f\omega}$ and the Stokes number $\lambda = b/\delta$ can be found. For a single beam with $s_1 = 80 \mu\text{m}$ and $s_2 = 24 \mu\text{m}$, taking $f = 21.18$ kHz and $\omega = 2\pi f = 133.08 \times 10^3$ rad/s, $R = b/2$, we get $\delta = 15.01 \mu\text{m}$. Using the above values, the Knudsen numbers $\text{Kn}_h = \lambda_a/h_1 = 0.0011$ and $\text{Kn}_b = \lambda_a/b = 0.0017$ with $b = 40 \mu\text{m}$ signify that the flow is in the continuum regime under ambient conditions. For $\text{Kn}_\delta = \lambda/\delta = 0.0045$, we get Weissenberg number $\text{Wi} = \omega\tau = (\text{Kn}_\delta)^2 = 2 \times 10^{-5} \ll 1$, which signifies that the flow can be considered as a quasisteady flow. However, the computation of Reynolds numbers $\text{Re}_h = \rho_f \omega h_1^2 / \mu \approx 32$ and $\text{Re}_b = \rho_f \omega R^2 / \mu = \rho_f \omega b^2 / 4\mu = b^2 / 2\delta^2 \approx 3.55$ and Stokes number $\lambda = b/\delta = 2.66$ shows that the inertial effect is important and needs to be considered accurately.

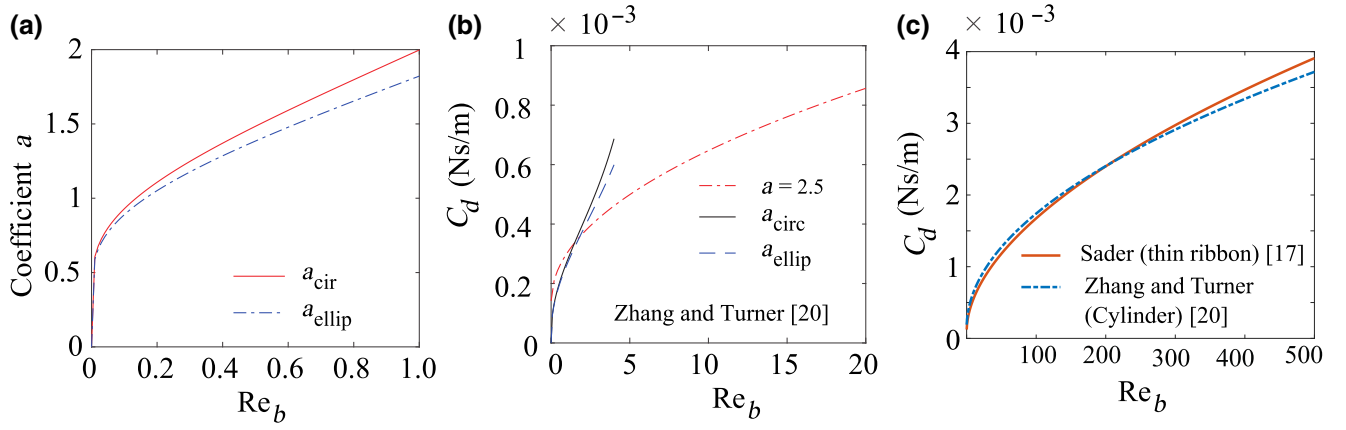


FIG. 3. (a) Variation of coefficient a in the damping coefficient for circular or elliptical section with Reynolds number for $Re_b \leq 1$. (b) Variation of damping coefficient $C_d = (2.5 + 2\lambda)\pi\mu$ with Reynolds number for $Re_b > 1$. (c) Comparison of damping coefficients based on Zhang and Turner [20] and on Sader [17].

III. ANALYTICAL MODEL

To compute the drag force due to flexural motion of a microcantilever beam, we derive the drag-force formula by following the approach described by Zhang and Turner [20] due to the sinusoidal motion of a rigid cylinder. Under the assumption of incompressible and laminar flow, the net fluid force per unit length due to normal pressure, radial shear, and angular shear stress of rigid cylinder can be written as [20]

$$f = \left[\left(\frac{5}{2} + 2\lambda \right) - i \left(2\lambda + \frac{\lambda^2}{2} \right) \right] \pi \mu U_{\max}, \quad (8)$$

where $i = \sqrt{-1}$, U_{\max} is the maximum velocity amplitude, $\lambda = 2R/\delta$ is a dimensionless number also called the Stokes number, $\delta = \sqrt{2\mu/\rho\omega}$ is called the penetration depth, μ is the fluid viscosity, ρ is the fluid density, ω is the angular frequency of an oscillating rigid cylinder, and R is taken as cylinder radius or $2R = b$ as the width of the rectangular beam. Consequently, $\lambda = b/\delta = \sqrt{2Re_b}$, which is a function of penetration depth or Reynolds number Re_b or frequency. The above expression becomes invalid for $\lambda \ll 1$, $Re_b \ll 1$, or $\omega \rightarrow 0$. To account for pseudostatic flow, the above expression can be modified based on Oseen's static flow [20] as

$$f = \left[(a + 2\lambda) - i \left(2\lambda + \frac{\lambda^2}{2} \right) \right] \pi \mu U_{\max}, \quad (9)$$

where a is the coefficient corresponding to Oseen's static flow results. For $Re_b < 1$, $a = a_{\text{cir}} = 4.0/[0.577 - \log(Re_b/8)]$ for a circular section and $a = a_{\text{ellip}} = -4.0/[0.577 + \log(Re_b/16)]$ for a thin elliptical section. The variation of these two parameters can be shown in Fig. 3(a) with frequency or Re_b . For $Re_b > 1$, $a = 5/2 = 2.5$ as given by Eq. (8). The net force from Eq. (8) consists

of damping and added mass effect. Taking the real component of net force, $f_d = \left(\frac{5}{2} + 2\lambda \right) \pi \mu U_{\max}$, the drag-force coefficient per unit length can be written as

$$C_d = \frac{f_d}{U_{\max}} = \left(\frac{5}{2} + 2\lambda \right) \pi \mu. \quad (10)$$

Similarly, the damping coefficients per unit length based on Sader's model can be found based on considering a beam with a thin ribbon [17]. Figure 3(b) shows the comparison of damping coefficient C_d with $a = 2.5$ based on Zhang and Turner [20] with C_d with $a = a_{\text{c}}$ and $a = a_{\text{ellip}}$. Furthermore, on comparing the damping coefficients C_d with $a = 2.5$ based on circular cylinder and C_{ds} based on Sader's results with a thin ribbon [17], we find nearly similar results even for large values of $Re_b \gg 1$ as shown in Fig. 3(c). However, it is also noted that the percentage difference decreases exponentially with Reynolds number. Since our objective is to propose a simple model, we take the analytical model given by Eq. (10) based on a circular cylinder. The corrections can be incorporated by multiplying the result by a factor associated with a rectangular section as proposed by Basak and Raman [22].

The above formula is valid for sinusoidal motion of a rigid cylinder or approximately for a beam with rectangular section when the velocity amplitude is constant along its length. We now derive the expression for the damping coefficient due to first bending mode of cantilever with assumed mode shape $(x/L)^2$ in which the velocity amplitude varies along its length.

To find the drag force, F_d , due to nonuniform motion of a cantilever, we take the drag force per unit length over a small section dx at a distance x from the fixed end of a cantilever beam of length L as

$$\frac{dF_d}{dx} = \left(\frac{5}{2} + 2\lambda \right) \pi \mu U_{\max}. \quad (11)$$

Consequently, the drag force on a small section of a beam is given by

$$dF_d = \left(\frac{5}{2} + 2\lambda \right) \pi \mu U_{\max} dx. \quad (12)$$

Taking the mode shape of a cantilever cylindrical beam as $\phi(x) = (x/L)^2$, the velocity distribution can be written as $u = A_{\max} \omega (x/L)^2 \sin(\omega t)$. Taking the maximum velocity $U_{\max} = V_{\max} (x/L)^2$, where $V_{\max} = A_{\max} \omega$, and substituting it in Eq. (12), we get

$$dF_d = \left(\frac{5}{2} + 2\lambda \right) \pi \mu V_{\max} \left(\frac{x}{L} \right)^2 dx. \quad (13)$$

Finally, the total drag force can be found by integrating the above equation over the length of cantilever beam as

$$\begin{aligned} F_d &= \left(\frac{5}{2} + 2\lambda \right) \pi \mu V_{\max} \int_0^L \left(\frac{x}{L} \right)^2 dx \\ &= \frac{1}{3} \left(\frac{5}{2} + 2\lambda \right) \mu V_{\max} L. \end{aligned} \quad (14)$$

The corresponding coefficient of drag per unit length, C_{cd1} , can be written as

$$C_{cd1} = \frac{\mu}{3} \left(\frac{5}{2} + 2\lambda \right). \quad (15)$$

Subsequently, to find the quality factor, we require the effective mass of the cantilever beam based on its assumed mode shape. Using $\phi(x) = (x/L)^2$, we obtain $k_{\text{eff}} \approx 4EI/L^3$. Using $\omega = \sqrt{k_{\text{eff}}/m_{\text{eff}}}$, we get $m_{\text{eff}} = k_{\text{eff}}/\omega^2 = 0.33m$, where m is the total mass of the beam. Finally, the quality factor can be found using $Q = m_{\text{eff}}\omega/C_{cd1}$. Similarly, using the exact mode shape of the cantilever beam corresponding to its first transverse mode, we can compute drag forces. To find the corresponding quality factor, we use $k_{\text{eff}} = 3EI/L^3$ and $m_{\text{eff}} = k_{\text{eff}}/\omega^2 = 0.23m$.

IV. NUMERICAL MODEL

In this section, we present the procedure for computing drag forces the using numerical method in ANSYS. We first describe the optimization of a geometric model and procedure for computing forces for the flexural motion of a rectangular beam. Then we study the influence of side boundaries on the quality factor for a given structure. Finally, we compare the numerical solution with the analytical and experimental results.

A. Numerical procedure

To optimize the computation of drag forces in ANSYS, we optimize a 3D fluid model around a single

microcantilever beam of length $L = 200 \mu\text{m}$, width $b = 40 \mu\text{m}$, and thickness $h = 0.965 \mu\text{m}$ with side gaps s_1 and s_2 as shown in Fig. 4(a). The beam is separated from the bottom surface by h_1 . To develop the outer boundaries for the given structure, the upper volume is bounded by the side surfaces located at distance s_0 from the outer periphery of the cavity and the upper surface located at distance h_2 from the top surface of the beam such that the pressure difference becomes invariable as shown in Figs. 4(b) and 4(c). For the oscillatory motion of the cantilever beam with velocity condition $V = V_{\max} (x/L)^2 \sin(\omega t)$, where $V_{\max} = 0.001h_1\omega$, zero-velocity conditions on fixed surfaces and zero-pressure boundary conditions on surfaces above the beam as described in Figs. 4(b) and 4(c), the incompressible Navier-Stokes equation [30] is solved to obtain the pressure and velocity distribution. Although we perform the analysis under the assumption of incompressible flow, a small compressibility can also be provided by the bulk modulus of air. Additionally, the flow is considered isothermal. After meshing the domain with about 10^5 Fluid 142 elements, we simulate the solution under optimized parameters so as to get a converged and steady-state solution. Here, the normalized relative rate of change of pressure and velocities is maintained at around 10^{-2} . Other parameters are discussed subsequently. Figures 4(d)–4(g) show the cross-section view of the pressure distribution in single beams as well as arrays of two and three beams at a specific time of simulation. The corresponding velocity distribution is shown in Figs. 4(h)–4(k). In the next subsection, we present the procedure for computing drag forces.

B. Procedure of computing drag forces

To compute the drag forces due to the flexural motion of a beam, we first simulate the pressure distribution for given dimensions and properties. We integrate the normal pressure and wall shear around the beam over a given time interval to obtain the net force and its maximum amplitude, F_{\max} , at steady state. Figure 5(a) shows the variation of total forces around the cylinder and its scaled velocity with time under flexural motion of the cantilever beam. To compute the drag-force component and added mass effect, we first find the phase difference between the force and velocity as shown in Fig. 5(a). If t_f and t_v are the corresponding time when force and velocity become zero in their final cycle as shown in Fig. 5(a), we get the phase difference by first finding the time difference between force and velocity as $\Delta t = t_f - t_v$, and compute the phase difference as $\phi = \omega \Delta t$. Finally, we obtain the drag force from $F_d = F_{\max} \cos \phi$ and fluid loading effect from $F_l = F_{\max} \sin \phi$. The damping coefficient per unit length is obtained from $C_d = F_d/(V_{\max}L)$. Based on the values of damping coefficient, we now present the optimization of fluid domain.

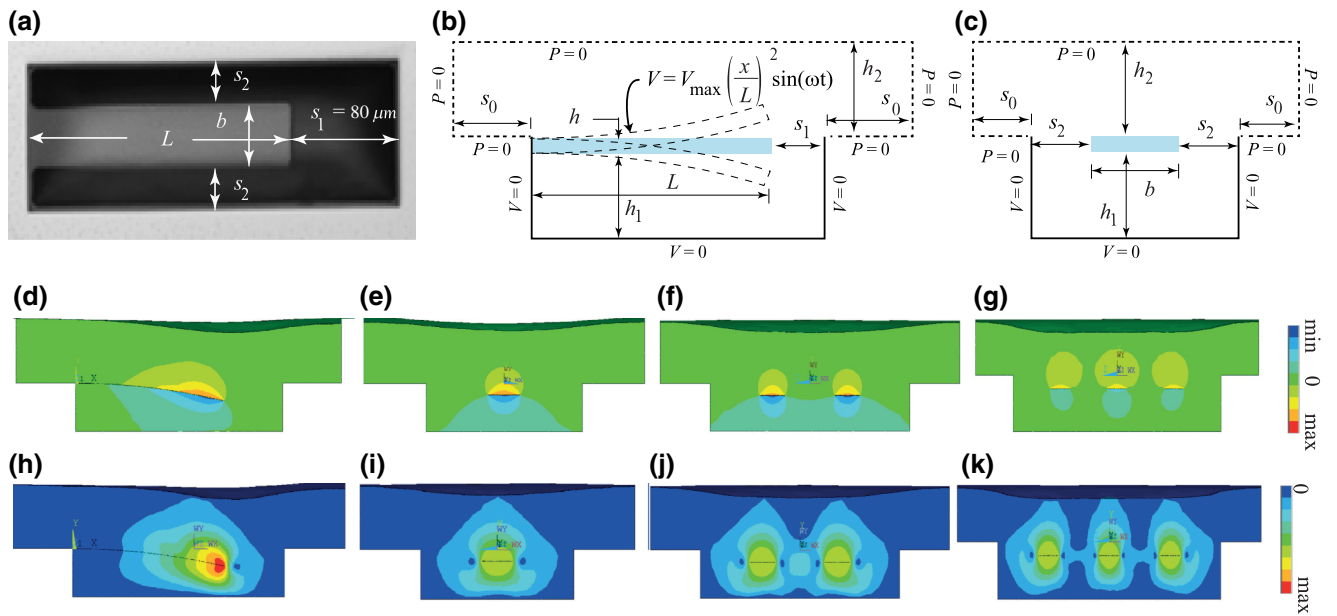


FIG. 4. (a) Top view of a single microcantilever beam with side boundaries. (a) Side and (b) end views of numerical fluid model around an oscillating cantilever beam bounded by the outer boundaries. Images of pressure distribution due to oscillating single beam for a section along its (d) length and (e) width. Pressure distribution on a section along the width of (f) two-beam array and (g) three-beam array. The corresponding velocity distributions are shown in (h)–(k) for single beams and arrays of two and three beams.

To minimize the numerical errors, it is essential to optimize the fluid domain and simulation parameters. We focus on optimizing the following parameters in a systematic process.

(a) For a given geometric domain and time step with $\lambda = 2.66$, we first optimize the number of elements, N_e , required to obtain a converged solution as shown in Fig. 5(b). It shows that as the number of elements increases from 8000 to 800 000, the damping coefficient changes from 1.66×10^{-4} to 1.26×10^{-4} . Therefore, we maintain the number of element as 10^5 to keep the numerical error associated with the number of elements negligible.

(b) The second important factor is the number of global staggered iterations per time step, N_s , in order to get converged solution in each step. Figure 5(c) shows the variation of the damping coefficient with the number of staggered iterations. It shows that the change in the damping coefficient is about 2% when N_s changes from 15 to 20. We take $N_s = 20$ in all our simulations to keep numerical error to less than 2%.

(c) The third important factor is the number of time steps, N_t , to obtain the steady-state solution. Figure 5(d) shows that the damping coefficient is nearly constant if N_t is kept greater than or equal to 15. We take $N_t = 20$ for all numerical simulations.

(d) The variation of the damping coefficient with the extended boundaries in Fig. 5(e) shows that the value becomes invariable if it is extended beyond 1.5 times the

width of the beam. Here, we take the ratio of distance of extended boundaries to beam width as 2 for all our numerical simulations.

(e) The variation of the damping coefficient with the bottom gap between the beam and fixed substrate in Fig. 5(f) shows that the damping coefficient remains constant when the gap to width ratio is more than 1.5. In the present case of test structures, $h_1 = 60 \mu\text{m}$ and $b = 40 \mu\text{m}$ lead a to gap to width ratio of 1.5.

C. Validation of numerical procedure

After optimizing the geometric and convergence-related parameters, we study the influence of oscillating frequency, in terms of Stokes number, λ , on the damping coefficient by comparing numerical results with the analytical model obtained in Sec. III. Figure 5(g) shows the comparison of damping coefficients obtained using numerical and analytical results at $\lambda = 2, 5$, and 10 corresponding to angular frequencies of 0.75×10^5 rad/s, 4.68×10^5 rad/s, and 18.75×10^5 rad/s, respectively. It shows that the analytical results agree well with the numerical results at low frequencies up to $\lambda = 5$. The percentage difference increases by around 40% at $\lambda = 10$. Since the frequency of our test structures is around 21.18 kHz which gives angular frequencies of 1.33×10^5 rad/s corresponding to $\lambda = 2.66$, the analytical model developed in the paper can be used for further analysis.

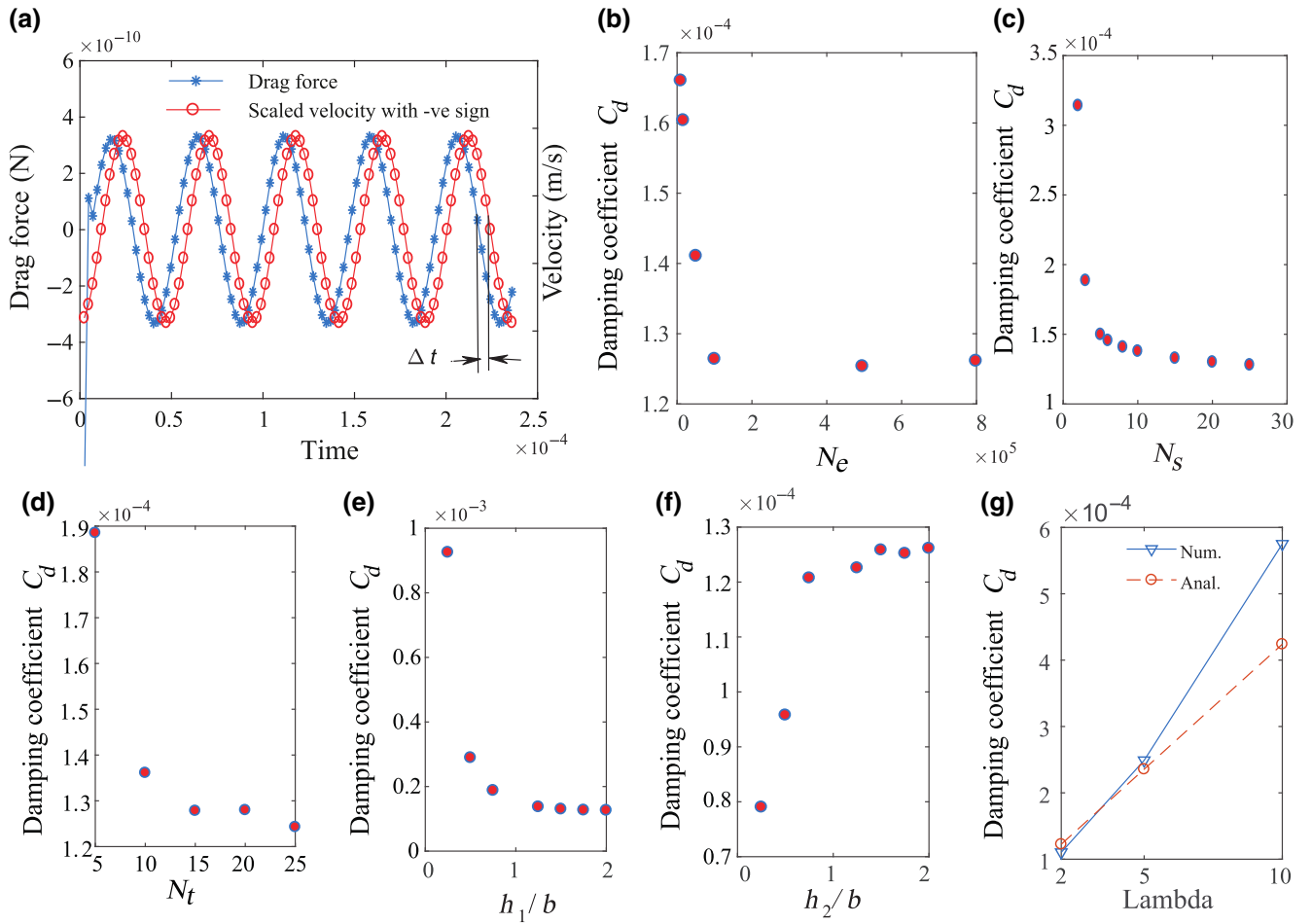


FIG. 5. (a) Time history of force and scaled velocity showing the time difference between total force and velocity. Variation of damping coefficient, C_d , with (b) number of elements, N_e , (c) number of global staggered iterations per step, N_s , (d) number of time steps, N_t , (e) bottom gap to beam width ratio, h_1/b , and (f) frequency parameter λ .

(a) *Squeeze film damping versus drag forces.* With the optimized numerical parameters, we analyze the influence of the air gap between oscillating beams with velocity $V = V_{\max} (x/L)^2 \sin(\omega t)$ and bottom substrate on squeeze film damping using Fluid 136 elements and total fluid damping (drag plus squeeze film) using Fluid 142 elements in Fig. 6(a). Squeeze film damping is found by solving the Reynolds equation using the modal projection method. Total fluid damping is found by solving the Navier-Stokes equation using Fluid 142 elements. In both cases, the fluid domain is bounded by the bottom substrate, the lower surface of the cantilever beam and end boundaries as shown in the inset of Fig. 6(a). The comparison of results suggests that the drag forces dominate over squeeze film as the gap thickness h_1 increases beyond 20 μm . Hence, we carry out further analysis using Fluid 142 elements.

(b) *Influence of boundary condition.* Consider the domain that bounds the cantilever beam from all sides with distance h_1 from the bottom substrate, h_2 from the top surface, s_0 from the left boundary, and s_1 from the

rest of the side boundaries. Taking $s_0 = s_1 = 80 \mu\text{m}$, we analyze the influence of the boundary on the quality factor when the bottom and top boundaries varies simultaneously as shown in Fig. 6(b). When we apply the zero-velocity condition on the bottom boundary and zero-pressure conditions on the rest of the boundaries, the quality factor increases to 50 μm (1.5 times that of beam thickness, h) and then becomes constant as the gap thicknesses $h_1 = h_2$ vary from 10 to 90 μm . Similarly, when we apply zero-pressure conditions on all the boundaries, the quality factor decreases to 40 μm (1.5 times the beam thickness, h) and then becomes constant as the gap thicknesses $h_1 = h_2$ vary from 10 to 90 μm . This shows that the influence of the lower and upper air gap can be completely neglected when the air-gap thickness is more than 60 μm . Under such conditions, squeeze film damping is completely neglected. The fluid damping is entirely due to drag forces. To further examine the effect, we vary only one of the gaps h_1 or h_2 while keeping other gap fixed at 80 μm under the zero-velocity condition on the bottom boundary and

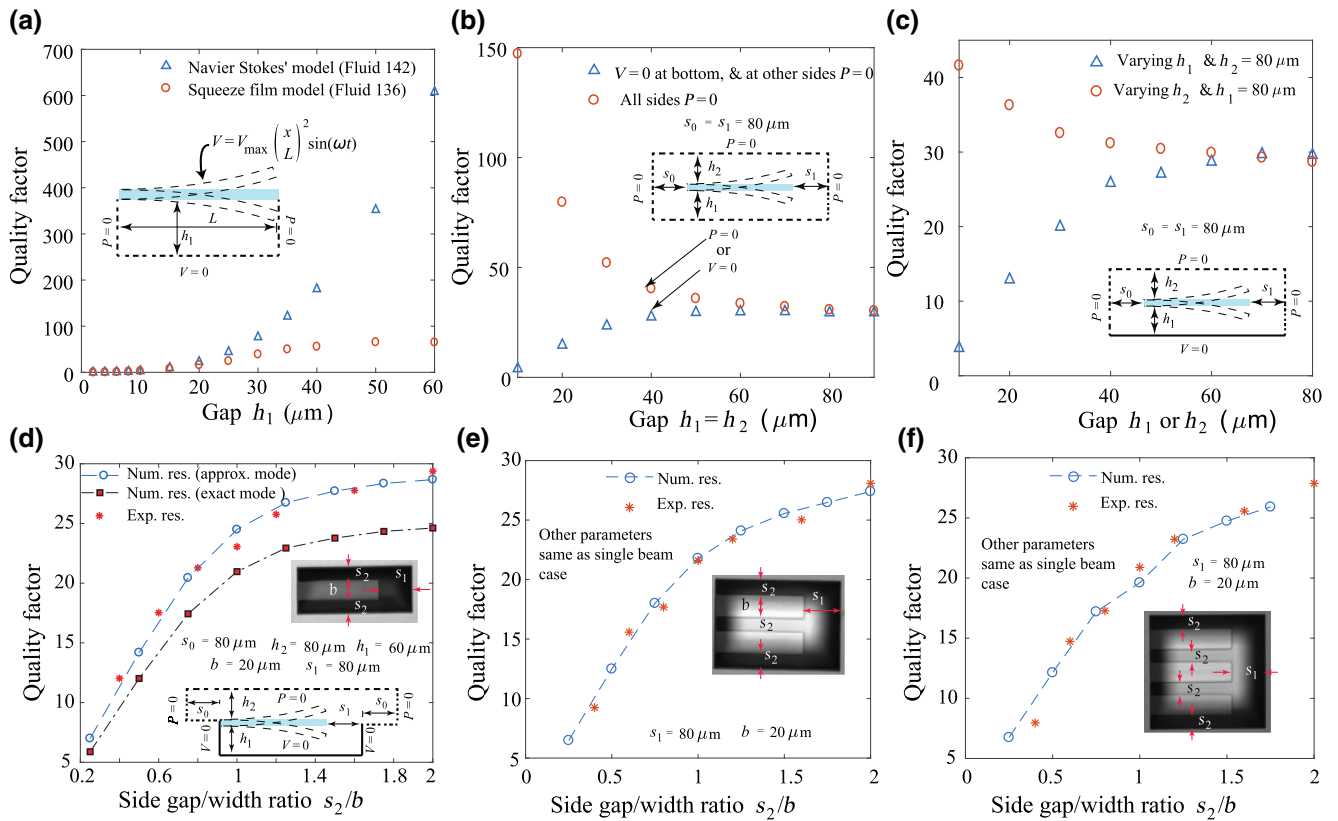


FIG. 6. Variation of quality factor (a) when fluid domain is limited to gap between oscillating beam and bottom substrate, (b) when fluid domain around oscillating beam is considered for the same bottom and top gap, $h_1 = h_2$, for a fixed position of side boundaries, and (c) when bottom h_1 or top h_2 boundary position changes for fixed h_2 or top h_1 and side boundaries. Comparison of numerical and experimental quality factor under actual boundary conditions of (d) single beam, (e) two-beam arrays, and (f) three-beam arrays.

zero-pressure conditions on the rest of the boundaries as shown in Fig. 6(c). This again proves that the fluid damping is entirely due to drag forces when the gap is beyond $60 \mu\text{m}$.

(c) *Influence of side gap of single beam.* To study the influence of side boundaries both with gap thickness s_2 on the quality factor of a single cantilever beam, we take the fluid domain around our test structure as shown in Figs. 4 and 6(d). Taking $s_0 = s_1 = 80 \mu\text{m}$, $h_1 = 60 \mu\text{m}$, $h_2 = 80 \mu\text{m}$, $L = 200 \mu\text{m}$, $b = 40 \mu\text{m}$, and thickness $h = 0.965 \mu\text{m}$, we vary the side gap s_2 to beam width b ratio on both sides of a single beam from 0.2 ($s_2 = 10 \mu\text{m}$) to 2 ($s_2 = 80 \mu\text{m}$). The numerical computation of the quality factor Q based on approximate mode shape and exact mode shape corresponding to transverse motion of the beam show that the boundary effect is quite significant up to $s_2/b \approx 1.5$, as shown in Fig. 6(d). Its effect starts diminishing as the side boundaries increase beyond it. Thus, the quality factor increases by 80% as the gap ratio varies from 0.25 to 2. Comparing the results with experimental results, we find the numerical approximation based on approximate mode shape works better than that with exact mode shape, perhaps due to the shape of fabricated beams.

Moreover, due to the simplicity of the approximate mode shape, we perform further analysis using $\phi(x) = (x/L)^2$.

(d) *Influence of interbeam gap of beam array.* To see the influence of the interbeam gap on the quality factor of beam arrays, we take two- and three-beam arrays as shown in Figs. 4 and 6(f), respectively. The comparison of numerical and experimental results reaffirms that the quality factor beyond an interbeam gap to beam width ratio of 1.5 becomes almost independent of the interbeam gap. Such inference is quite significant in controlling the fluid damping in arrays of beams.

V. MODIFIED ANALYTICAL MODEL FOR BEAM ARRAYS

In this section, we present a systematic simulation to modify the analytical formula presented in Sec. III in order to compute forces in an array of beams under different boundary conditions.

A. Side boundary-interbeam gap effect

To compute forces in an array of cantilevers oscillating with an assumed mode shape of $\phi(x) = (x/L)^2$, we

modify the formula obtained for a single beam under open boundary conditions from Eq. (15) to represent two specific boundary conditions as follows.

(i) *Boundary with two closed side walls located at same distance with $V = 0$.* Let us consider a boundary condition in which the beam is open from the top and closed at the bottom, and all the side boundaries. Taking the side boundaries as equidistant from the edge of the beam, we take the zero-velocity condition on the left and right side boundaries located at s_2 and bottom boundary located at $h_1 = 60 \mu\text{m}$, and the zero-pressure condition on the top boundary located at $h_2 = 80 \mu\text{m}$ to compute the drag forces as shown in Fig. 7(a). The zero-pressure condition is represented by the dashed line and the zero-velocity condition is represented by solid line around the beam. Figure 7(a) shows the variation of the damping coefficient with the gap, which can be approximated by the expression

$$C_{d1} = 8.9C_{d0} \exp \left[-4.2 \left(\frac{s_2}{b} \right) + 0.89 \right], \quad (16)$$

where $C_{d0} = (2.5 + 2\lambda)\pi\mu/3$ is the damping coefficient under open-boundary conditions. The above approximation captures the results over a large range of gap ratio.

(ii) *Boundary with one partially closed side wall and another closed side wall located at half the distance.* In this case, taking the top and bottom boundary condition to be same as those in previous case, we apply the zero-velocity condition at the inner right boundary located at $s_2/2$ distance from the beam edge, and zero-pressure and zero-velocity conditions on the outer boundary located at distance s_2 from the beam to compute the drag forces as shown in Fig. 7(b). It shows the variation of the damping coefficient with the ratio of the gap between the closed wall and the beam width b . Under this condition, we found that the damping reduces exponentially as the gap ratio, $r = s_2/b$. Approximating the variation with the exponential function, we find the modified formula

$$C_{d2} = 6.65C_{d0} \exp \left(-3.1 \left[\frac{s_2}{b} \right] + 0.93 \right). \quad (17)$$

Using the above formulas, we compute damping coefficients in arrays of two, three, and four beams, respectively,

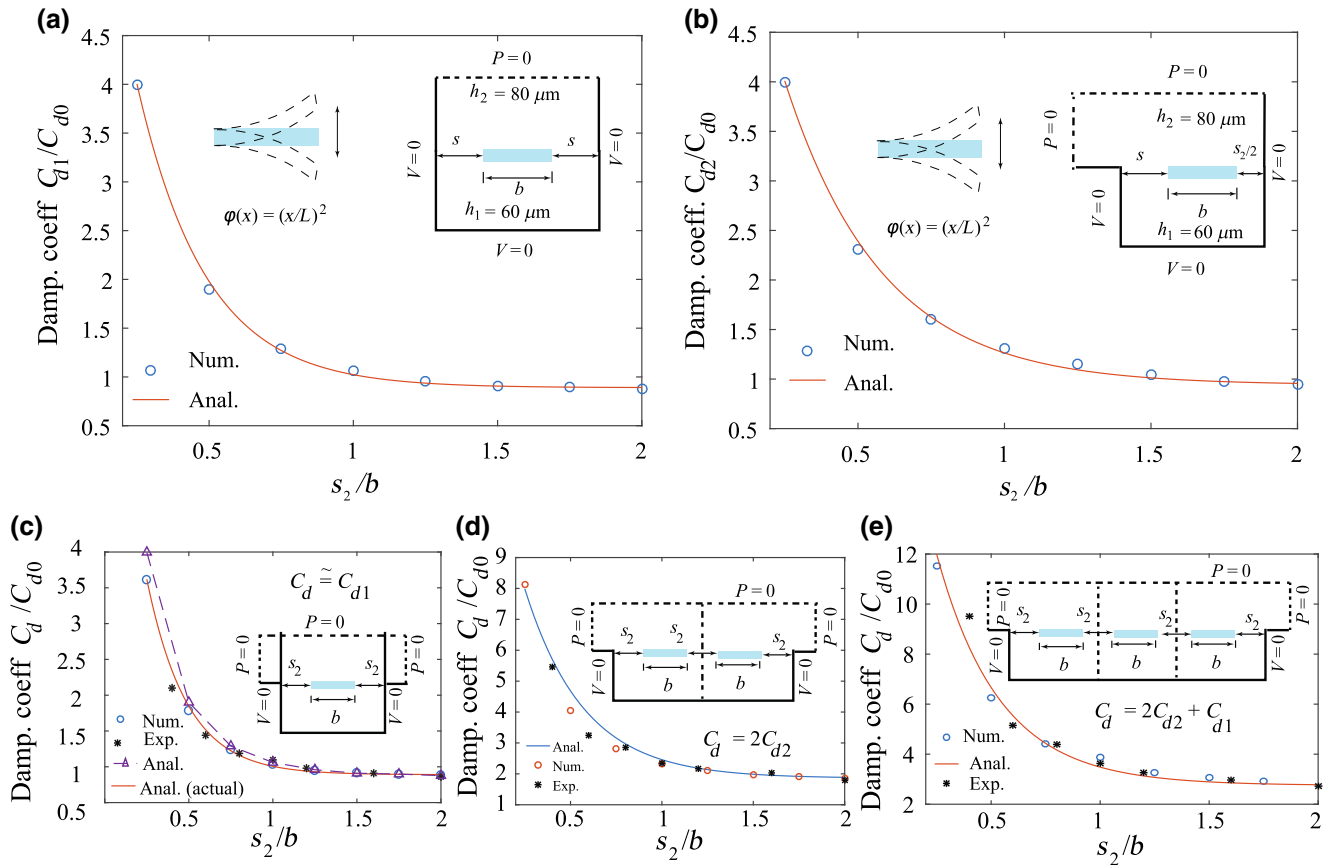


FIG. 7. Variation of drag coefficient with ratio of distance from side boundary, s_2 to beam width b (a) when both side boundaries are closed, (b) when one side boundary is partially closed and another is fully closed. Comparisons between numerical and approximate analytical models are presented for (c) single beam, (d) two-beam array, and (e) three-beam array.

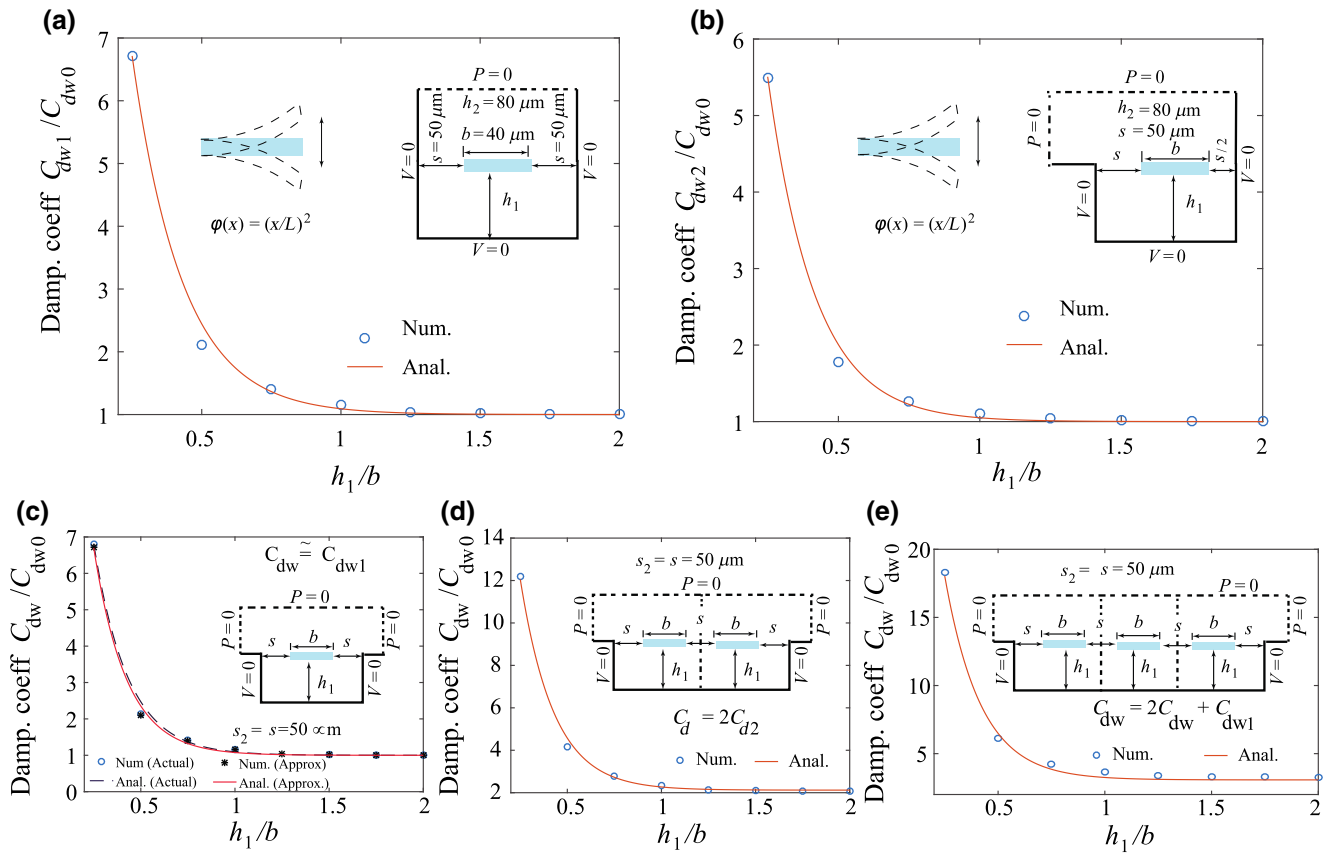


FIG. 8. Variation of drag coefficient with the ratio of distance from the lower wall, h_1 to beam width b , (a) when both side boundaries are closed, (b) when one side boundary is partially closed and another is fully closed. Comparison between numerical and approximate analytical models are presented for (c) single beam, (d) two-beam array, and (e) three-beam array.

by classifying the individual beams of an array into the sets of beams with the above two cases.

(iii) *Single beam.* Since the actual boundary condition of a single beam involves partially closed side boundaries located at a distance s_2 from the outer periphery of the beam as shown in Fig. 7(c), we compare the solutions obtained between the actual boundary condition and approximate conditions in which side boundaries are approximated as fully closed. Taking the top and bottom boundaries to be the same as the above cases, we compare the variation of drag forces versus the side gap to beam width ratio s_2/b for actual conditions and approximate conditions in Fig. 7(c). This shows that the damping coefficient C_d under actual conditions is approximately equal to that under approximate conditions, C_{d1} (i.e., $C_d \cong C_{d1}$). When the gap s_2 is large, the approximate formula gives similar results to that based on actual conditions. However, when the gap reduces, a percentage difference of around 14% is obtained.

(iv) *Two-beam array.* In this condition, each beam can be represented by a beam with one closed wall with half the gap $s_2/2$ as compared to other partially closed side boundary located at distance s_2 from beam edge. Hence,

the total damping coefficient, C_d , can be found by taking two times the damping coefficient C_{d2} (i.e., $C_d = 2C_{d2}$). Figure 7(d) shows the comparison between this approximation and the numerical solution. The approximate formula gives a maximum error of about 5%.

(v) *Three-beam array.* Similarly, in this condition, the two outer beams can be represented by a beam with one closed wall and another side with partially closed wall. The inner beam is represented by a beam with two closed walls. Hence, total damping coefficient, C_d , can be found as $C_d = 2C_{d2} + C_{d1}$. Figure 7(e) shows the comparison between this approximation and the numerical solution. The approximate formula gives a maximum error of about 12%.

B. Lower wall effect

To capture the lower wall effect on the drag coefficient of a single beam as well as array of beams, we first modify the formula under the open boundary conditions based on the numerical simulation. If the beam is located at a distance h_1 from the lower boundary, we get the following formulas under different boundary conditions.

(i) *Boundary with two side walls at same distance.* To capture the variation of the wall effect under the condition when two side boundaries are closed and located at a distance $s = s_2$ from beam edges, respectively, we vary the bottom gap to beam width ratio h_1/b from 2 to 0.25 when the side gap is $s = s_2 = 50 \mu\text{m}$. For a constant s , we find that the damping coefficient reduces exponentially as the h_1/b ratio increases as shown in Fig. 7(a). Hence, we obtain the formula to capture the lower wall effect on damping coefficient per unit length, $C_{\text{dw}1}$, as:

$$C_{\text{dw}1} = C_{\text{cd}1} \left\{ 24 \exp \left[-5.75 \left(\frac{h_1}{b} \right) \right] + 1 \right\}, \quad (18)$$

where $C_{\text{cd}1}$ is the damping coefficient without considering the lower wall effect. It is interesting to note that the presence of lower wall modifies the formula by a multiplication factor $\xi_1 = \{24 \exp[-5.75 (h_1/b)] + 1\}$.

(ii) *Boundary with one partially closed side wall at distance s and closed wall at distance $s/2$.* Similarly, to capture the influence of the bottom gap on the damping coefficient for the case in which the partially closed boundary is located at $s = s_2$ and the fully closed boundary is located at $s/2$ from the beam, we vary the bottom gap to beam width ratio h_1/b from 0.25 to 2 for a constant side gap $s = s_2 = 50 \mu\text{m}$. The variation of the damping coefficient versus h_1/b , which is shown in Fig. 8(b), can be captured by modifying the formula as follows:

$$C_{\text{dw}2} = C_{\text{cd}2} \left\{ 20.2 \exp \left[-6.0 \left(\frac{h_1}{b} \right) \right] + 1 \right\}, \quad (19)$$

where $C_{\text{cd}2}$ is the damping coefficient without considering the lower wall effect. The multiplication factor is found to be $\xi_2 = \{20.2 \exp[-6.0 (h_1/b)] + 1\}$.

It is also found that the effect of the lower wall on the drag coefficient for boundary condition under which two closed side boundaries at the same distance from the beam edge can be captured by simply multiplying the corresponding formulas from Eqs. (16) by the multiplication factor ξ_1 . Similarly, the effect of the lower wall on the damping coefficient under other boundary conditions consisting of one partially closed boundary and one closed boundary can be found by multiplying the formulas by multiplication factor ξ_2 .

To capture the influence of the bottom gap h_1 on the damping coefficient for a single beam, we approximate two boundary conditions as closed in place of actual partially closed boundary conditions. Comparing the numerical results and analytical model under actual boundary conditions with an approximate model with closed boundary conditions (i.e., $C_d = C_{d1} \xi_1$) as shown in Fig. 8(c), we find that both models approximate the numerical results

without introducing much error. Similarly, to show the effect of the bottom gap on the damping coefficient of two-beam arrays, we take $C_d = 2C_{\text{dw}2} = 2C_{d2} \xi_2$. Comparing with the numerical solution as shown in Fig. 8(d), we find a maximum percentage error of around 9%. In the case of three-beam arrays, the damping coefficient can be approximated as $C_d = 2C_{\text{dw}2} + C_{\text{dw}1} = 2C_{d2} \xi_2 + C_{d1} \xi_1$ with a maximum percentage error of about 10% with respect to the numerical results as shown in Fig. 8(e).

At the outset, we stated that model presented in this paper can be effectively used to model drag forces near or away from bottom substrate or nearest neighbor. It is found that if the interbeam gap to beam width ratio is greater than 1.5, the coupling effect of the neighboring beams can be negligible. Although the effect of higher frequency can be captured through the Stokes number λ , we present the results for $\lambda = 2.66$. However, the present model can be verified for higher frequencies.

VI. CONCLUSIONS

In this paper, we present experimental, analytical, and numerical drag-force analyses for MEMS-based beams. We first fabricate single beams as well as arrays of two and three MEMS cantilever beams with different side gaps or interbeam gaps. We measure the frequency and quality factor under ambient conditions. To systematically arrive at an appropriate analytical model, we approximate the mode shape and derived the drag-force formula for cantilever beams. Then we develop a numerical model to compute the drag forces in the above structures. After optimizing the numerical parameters such as the number of elements, the number of global staggered iterations per time step, the number of time steps per cycle, and the domain boundaries, we compute numerical values of drag forces due to flexural motion of the cantilever beam. We find that the analytical results match well the numerical results at low frequencies. After validating the numerical model and its comparison with developed analytical models and experiments for different boundary conditions, we modify them in order to compute the drag forces in arrays of two, three, and four beams. The modified analytical models are found to be effective in computing the drag forces in arrays with percentage errors of between 5% and 12%. Moreover, to capture the effect of the lower wall, we introduce a multiplication factor to modify the analytical model based on numerical results. The modification is found to be useful in computing drag forces in single beams as well as arrays of beams, with percentage error between 9% and 10%. Finally, we conclude that the formulas developed in the paper by modifying the fundamental analytical model can act as handy design tools in the designs of sensors and actuators based on MEMS arrays.

ACKNOWLEDGMENT

This work was partially supported by Grant No. CSIR 22(0696)/15/EMR-II.

- [1] G. Popescu, The power of imaging with phase, not power, *Physics Today* **70**, 34 (2017).
- [2] D. Guan, E. Charlaix, R. Z. Qi, and P. Tong, Noncontact Viscoelastic Imaging of Living Cells Using a Long-Needle Atomic Force Microscope with Dual-Frequency Modulation, *Phys. Rev. Applied* **8**, 044010 (2017).
- [3] P. N. Kambali, G. Swain, A. K. Pandey, E. Buks, and O. Gottlieb, Coupling and tuning of modal frequencies in direct current biased microelectromechanical systems arrays, *Appl. Phys. Lett.* **107**, 063104 (2015).
- [4] Z. Wen, L. Deng, X. Zhao, Z. Shang, C. Yuan, and Y. She, Improving voltage output with PZT beam array for MEMS-based vibration energy harvester: Theory and experiment, *Microsyst. Technol.* **21**, 331 (2015).
- [5] D. A. Walters, J. P. Cleveland, N. H. Thomson, P. K. Hansma, M. A. Wendman, G. Gurley, and V. Elings, Short cantilevers for atomic force microscopy, *Review of Scientific Instruments* **67**, 3583 (1996).
- [6] A. Schneider, R. H. Ibbotson, R. J. Dunn, and E. Huq, Arrays of SU-8 microcantilevers with integrated piezoresistive sensors for parallel AFM applications, *Microelectron. Eng.* **88**, 2390 (2011).
- [7] S. Somnath, H. J. Kim, H. Hu, and W. P. King, Parallel nanoimaging and nanolithography using a heated microcantilever array, *Nanotechnology* **25**, 014001 (2014).
- [8] M. Seong, S. Somnath, H. J. Kim, and W. P. King, Parallel nanoimaging using an array of 30 heated microcantilevers, *RSC Adv.* **4**, 24747 (2014).
- [9] J. P. Maris, L. Aeschimann, A. Meister, R. Ischer, E. Bernard, T. Akiyama, M. Giazon, P. Niedermann, U. Staufer, R. Pugin, N. F. de Rooij, P. Vettiger, and H. Heinzelmann, Piezoresistive scanning probe arrays for operation in liquids, *J. Phys. Conf. Ser.* **61**, 955 (2007).
- [10] H. Hasaka, K. Itao, and S. Kuruda, Damping characteristics of beam-shaped micro-oscillators, *Sens. Actuator. A Phys.* **49**, 87 (1995).
- [11] L. D. Landau and E. M. Lifshitz, *Fluid Mechanics* (Pergamon Press, Oxford, 1987).
- [12] T. Ikehara, J. Lu, M. Konno, R. Maeda, and T. Mihara, A high quality-factor silicon cantilever for a low detection-limit resonant mass sensor operated in air, *J. Micromech. Microeng.* **17**, 2491 (2007).
- [13] S. S. Verbridge, R. Ilic, H. G. Craighead, and J. M. Parpia, Size and frequency dependent gas damping of nanomechanical resonators, *Appl. Phys. Lett.* **93**, 013101 (2008).
- [14] S. D. Vishwakarma, A. K. Pandey, J. M. Parpia, S. S. Verbridge, H. G. Craighead, and R. Pratap, Size modulated transition in the fluid-structure interaction losses in nano mechanical beam resonators, *J. Appl. Phys.* **119**, 194303 (2016).
- [15] W. E. Newell, Miniaturization of tuning forks, *Science* **161**, 1320 (1968).
- [16] E. C. Bullard, J. Li, C. R. Lilly, P. Mulvaney, M. L. Roukes, and J. E. Sader, Dynamic Similarity of Oscillatory Flows Induced by Nanomechanical Resonators, *Phys. Rev. Lett.* **112**, 015501 (2014).
- [17] J. E. Sader, Frequency response of cantilever beams immersed in viscous fluids with applications to the atomic force microscope, *J. Appl. Phys.* **84**, 64 (1998).
- [18] A. Maali, C. Hurth, R. Boisgard, Cédric Jai, T. Cohen-Bouhacina, and J.-P. Aimé, Hydrodynamics of oscillating atomic force microscopy cantilevers in viscous fluids, *J. Appl. Phys.* **97**, 074907 (2005).
- [19] X. Xia and X. Li, Resonance-mode effect on microcantilever mass-sensing performance in air, *Rev. Sci. Instrum.* **79**, 074301 (2008).
- [20] W. Zhang and K. Turner, Frequency dependent fluid damping of micro/nano flexural resonators: Experiment, model and analysis, *Sens. and Act., A* **134**, 594 (2007).
- [21] W. Zhang, M. Requa, and K. L. Turner, *Proceedings of Material Science* (2006), pp. 1–4.
- [22] S. Basak and A. Raman, Hydrodynamic coupling between micromechanical beams oscillating in viscous fluids, *Phys. Fluids* **19**, 017105 (2007).
- [23] A. Ashok, P. Manoj Kumar, S. S. Singh, P. Raju, P. Pal, and A. K. Pandey, Achieving wideband micromechanical system using coupled non-uniform beams array, *Sens. Actuator. A: Phys.* **273**, 12 (2018).
- [24] V. Gattulli, F. Potenza, and M. Lepidi, Damping performance of two simple oscillators coupled by a visco-elastic connection, *J. Sound Vib.* **332**, 6934 (2013).
- [25] G. Dolfo and J. Vigué, Damping of coupled harmonic oscillators, *Eur. J. Phys.* **39**, 025005 (2018).
- [26] D. F. Wang, K. Chatani, T. Ikehara, and R. Maeda, Mode localization analysis and characterization in a 5-beam array of coupled nearly identical micromechanical resonators for ultra-sensitive mass detection and analyte identification, *Microsyst. Technol.* **18**, 1923 (2012).
- [27] H. Yabuno, Y. Seo, and M. Kuroda, Self-excited coupled cantilevers for mass sensing in viscous measurement environments, *Appl. Phys. Lett.* **103**, 063104 (2013).
- [28] L. Meirovitch, *Fundamentals of Vibrations* (McGraw-Hill, Boston, 2001).
- [29] J. B. Schwarz and H. M. Richardson, *Proceedings of Engineering* (CSI Reliability Week, Orlando, FL, 1999).
- [30] A. K. Pandey, R. Pratap, and F. S. Chau, Influence of boundary conditions on the dynamic characteristics of squeeze films in MEMS devices, *J. Microelectromech. Syst.* **16**, 893 (2007).